Expert Systems With Applications 293 (2025) 128681

Contents lists available at ScienceDirect

Expert Systems With Applications

journal homepage: www.elsevier.com/locate/eswa

A hybrid deep learning approach for enhancing the Lorentzian curve fit algorithm for Schumann resonance

Carlos Cano-Domingo [a,b], Ruxandra Stoean [c,d,e,*], Gonzalo Joya [f], Nuria Novas [g], Manuel Fernández-Ros [g], Jose A. Gázquez Parra [g]

[a] Department of Computer Science, Universitat Politecnica de Catalunya, Carrer de Jordi Girona, 31, Les Corts, Barcelona, 08034, Spain
[b] Barcelona Supercomputing Center (BSC-CNS), Plaça Eusebi Güell, 1-3, Barcelona, 08034, Spain
[c] Department of Computer Science, University of Craiova, A. I. Cuza 13, Craiova, 200585, Romania
[d] Artificial Intelligence and Machine Learning, Romanian Institute of Science and Technology, Saturn 24-26, Cluj-Napoca, 400504, Romania
[e] Department of Computer Science, West University of Timişoara, V. Pârvan 4, Timişoara, 300223, Romania
[f] Departamento Tecnologia Electronica, Universidad de Malaga, Campus de Teatinos, Malaga, 29071, Spain
[g] Ceia3, Departamento de Ingenieria, Universidad de Almeria, Ctra. Sacramento s/n, Almeria, 04120, Spain

ARTICLE INFO

Keywords:
Deep learning
Autoencoder
Convolutional neural network
Schumann resonance
Extremely low frequency
Lorentzian fit

ABSTRACT

Schumann Resonance (SR) represents a set of very weak signals formed by the electromagnetic wave propagation along the Earth-ionosphere cavity. Traditionally, SR studies have focused on extracting only their first mode using the average frequency spectrum over long segments. However, advances in sensor technology and digitalization now allow for the analysis of multiple modes, which can significantly enhance our understanding and characterization of SR signals. Even in this context, standard techniques, such as Lorentzian Curve Fit (LCF), often fail to retain the characteristics of the signal when the multiple modes are included, especially under harsh weather conditions. This limitation arises from the mathematical challenges of fitting procedures over noisy, highly variable signals, which become more pronounced when extracting more than three modes. In this paper, we put forward a solution to this problem. Its novelty stems from a Deep Learning (DL) methodology based on three different autoencoder strategies and two learning schemes to denoise signals, handle multiple SR modes simultaneously, while adapt to their non-stationarity and variability. The results demonstrate that the DL model achieves high performance even when fitting a Lorentzian function is impossible, by effectively extracting multiple SR modes under challenging conditions. This outcome provides compelling evidence for further investigation into the use of DL data reduction techniques for analyzing SR signals.

1. Introduction

SR (Schumann, 1952) is composed of very weak electromagnetic signals resulting from the propagation of the corresponding waves within the Earth-ionosphere cavity. In addition to gaining insight into its behavior, in the last few years, SR has been attracting increasing interest in its connection with other natural phenomena, further affecting human lives and systems (Hetita et al., 2022). The relationship with lightning discharges has been widely investigated because it is the primary source of energy dissipated by the SR. Another main area of interest is the usage of SR experimental data in their potential relationship to seismic activity.

On the expert system side, since its advent, DL has multiplied its popularity in various areas of application. The particular use of DL for signal processing has also been gaining a lot of attention. Such research works point out the possibility of using advanced computing algorithms, specifically DL, to improve the traditional SR methodologies. To the best of our knowledge, no previous study has applied DL techniques directly to SR signals—either for signal processing or information extraction. In our recent work (Cano-Domingo et al., 2022), an initial step is taken by extracting a large set of time-domain characteristics from SR transient events (rather than frequency-domain registers) to serve as input for subsequent machine learning or DL models; nevertheless, that contribution is limited to the feature extraction stage.

The traditional or adapted LCF approaches to SR fight intensely with its weak and noisy signals, with overlapping spectral lines for multiple-mode analysis, and with a non-stationary and highly variable behavior in these signals. This research gap is what we intend to fill with the current approach.

The global hypothesis of this paper is that we assume that the LCF function performs in very good terms when it comes to a SR register with a small quantity of noise. In that case, both the frequencies extracted and

* Corresponding author.
E-mail address: ruxandra.stoean@inf.ucv.ro (R. Stoean).

https://doi.org/10.1016/j.eswa.2025.128681
Received 19 February 2025; Received in revised form 17 June 2025; Accepted 17 June 2025
Available online 20 June 2025

the output characterize the SR in an extremely precise way. However, when the SR raw signal is not clear enough, the extracted values and the LCF curve cannot be considered as an accurate representation of the real SR signal.

The proposed DL methodology exploits the assumption that all Extremely Low Frequency (ELF) registers comprise the true SR signal. It is thus supposed that the system learns from an utterly representative sample space of all types of SR signals, although only ELF registers with low noise have been considered for the training part. These registers can be perfectly labeled, frequencies extracted and LCF curve obtained, and then fed to the DL model.

It may be thought that the use of a deep regression would be enough for the purpose of this research. Nevertheless, the frequency regression has to be applied to a processed version of the input, in which the main features remain available, even where there has been a substantial reduction of inherent variability. This is why we put forward a novel AutoEncoder (AE) scheme, where the learned space is utilized to extract the central characteristics of the output.

This study therefore has two main objectives. The primary step is the development of a DL framework applied for the SR. Secondly, we take a fresh look at the procedure for the extraction of central frequencies for SR, focusing on a new methodology that does not need a middle stage as the LCF. In this respect, we introduce a novel component of the loss function that minimizes the error between the estimate and the real LCF.

The originality of the proposed DL approach thus comes from several facets. First, DL models, particularly AE, can learn to denoise signals and extract underlying patterns despite high noise levels. Second, the methodology can handle multiple resonance modes simultaneously, effectively disentangling overlapping spectral features without the need for separate fitting procedures for each mode. Third, a DL model can capture temporal dynamics and adapt to non-stationary behavior in the data, improving the accuracy of feature extraction over varying conditions. Last, but not least, the approach reduces the need for manual sample discarding by effectively processing data segments, previously unusable due to noise and variability. Furthermore, a recent study (Oppliger et al., 2024) demonstrates the effectiveness of using a deep Artificial Neural Network (ANN) to denoise very weak signals in the context of X-ray diffraction, suggesting that similar techniques could be beneficial for SR signal analysis.

This paper is organized as follows. Section 2 positions the current research in the literature context. The novel features of the approach are highlighted in Section 3. Section 4 describes the methodology employed, focusing on the description of the three DL AE methods and the two options to learn the reconstruction part. It also provides a description of the data set utilized, as well as an estimate of the computational complexity of the approach. The results, along with their interpretation, are presented in Section 5. Section 6 compares the proposed technique with a direct Convolutional Neural Network (CNN) model application on the samples. An overall discussion on the approach, with its limitations and possible applications, is presented in Section 7. Conclusions are drawn in the final section.

2. Related work

Since the discovery of SR around 70 years ago, many studies (Kudintseva et al., 2018; Perotoni, 2018) have developed a theoretical framework for its characterization. Bozóki et al. (2021) explored electromagnetic simulations with promising results. The examination of regular variations in SR intensity and frequency in different locations was carried out with a similar approach in Spain (Cano-Domingo et al., 2021), Greece (Tatsis et al., 2021) and the UK (Pizzuti et al., 2022).

Regarding the SR relationship with natural phenomena, Tatsis et al. (2021) studied the effect of lightning activity in a single observatory located in Greece, while Koloskov et al. (2020) examined 10 years of measurements using two distant observatories (Arctic and Antarctic). Boldi et al. (2018) reconstructed lightning activity using SR experimental data. Figueredo et al. (2021) highlighted the association between SR registers and large earthquakes in Mexico, using a signal time window surrounding the occurrence of the event. Hayakawa et al. (2021) also studied the connection of the SR signal with two massive earthquakes in Japan. An analysis model of SR related to earthquakes (Galuk et al., 2020) reveals causative modifications in the spectra.

Classical studies on SR have primarily focused on analyzing the first resonance mode, due to technological limitations in sensor sensitivity and data processing capabilities. Recent advances in sensor systems and digital tools have enabled the investigation of additional modes, leading to significant findings that support previously hypothesized relations with phenomena such as transient luminous effects (Qiu et al., 2024), volcanic activity (Shvets et al., 2024), and earthquakes (Contopoulos et al., 2024).

However, the methods used to extract the main characteristics of the SR signal are still based on traditional techniques, notably the LCF applied to aggregated frequency transformations over periods of 10 or 30 min. The LCF algorithm faces nevertheless significant challenges when dealing with SR data due to a number of impediments. SR signals are inherently weak and susceptible to various sources of noise, including atmospheric disturbances and instrumentation. The LCF struggles to accurately fit the resonance peaks when the signal-to-noise ratio is low, often leading to unreliable or invalid results. In addition, as more resonance modes are analyzed, the overlying of spectral lines becomes more pronounced, complicating the fitting process. Rodríguez-Camacho et al. (2022) showed that the LCF was thus less effective when multiple modes were present, especially beyond the first three, because of increased peak broadening and overlap. SR signals also exhibit high variability and non-stationary behavior over time (Nickolaenko et al., 2024), influenced by factors such as diurnal cycles and weather conditions. The LCF conversely assumes a stationary signal over the aggregation period, which may not hold true, leading to inaccuracies. Due to these constraints, certain data segments cannot be effectively analyzed using LCF and must be manually discarded. This reduces the amount of usable data and may exclude important information related to specific geophysical events.

All these limitations consequently hinder the ability to fully utilize the available SR data, especially when attempting to study correlations with other phenomena under noisy conditions. On the other hand, DL has been successfully employed in numerous signal processing tasks. Purwins et al. (2019) reviewed DL models for audio processing, in relation to speech, music and environmental sound detection and synthesis. Fime et al. (2024) predicted danger from audio signals of Android using several noise reduction techniques in combination with various CNN and transformer models. A deep ANN (Pamukti et al., 2024) assesses the curvature of a bent optical fiber. A CNN model (Ribeiro et al., 2020) analyzes ECG signals to recognize several types of cardiological abnormalities. Another CNN architecture (Ganguly & Dey, 2024) also inspects ECG signals for the detection of sleep apnea. A CNN - LSTM (Stoean et al., 2020) diagnoses presymptomatic cases of spinocerebellar ataxia from EOG signals. DL also emerges as a natural solution to improve feature extraction (Gao et al., 2023; Kim et al., 2023; Yang et al., 2019), when classical methodologies struggle to operate, particularly in the presence of noisy and complex data. With the support of DL techniques, we aim to address the specific challenges of the LCF algorithm by providing a more robust and automated method for extracting characteristics from weak and noisy SR signals.

The use of LCF as part of the methodology (Cano-Domingo et al., 2021, 2023; Guha et al., 2017; Tatsis et al., 2021) allows a global comparison between experimental data in different locations. However, some preliminary work to improve the performance of this algorithm was performed several years ago. In this sense, Mushtak and Williams (2009) developed an improved version of the LCF and Ondrášková and Ševčík (2014) created a complex demodulation algorithm. Although these approaches are interesting, they could not overcome the problems related to the extreme variability of the signal, the intense noise in the

ELF band, and also the mathematical problems of any fitting procedure (Maddams, 1980).

Therefore, the incorporation of a DL model into SR signal processing is expected to overcome the limitations of traditional LCF methods, improve the extraction of meaningful features from the data, and enable the analysis of previously unusable segments. This enhancement could lead to a better understanding and characterization of SR signals and their correlations with various geophysical phenomena.

The AE (Li et al., 2023) we use as the backbone of our methodology is an ANN that is used to learn efficient encodings of unlabeled data. The architecture is trained using the same signal in the input as in the desired output. The system reduces the dimension of the signal to codify the most useful information in a learned space. The cost function mainly comprises the error between the system input (expected output) and the decoded output. Therefore, the AE is forced to restore the input with a reduced dimension number, typically at least 20 times less. AE has demonstrated promising results for denoising purposes, e.g., in ultrasound signals (Gao et al., 2020), radar signals (Qu et al., 2019), PPG signals (Mohagheghian et al., 2024) and spatiotemporal features in videos (Ul Amin et al., 2024). In the Variational AutoEncoder (VAE) version, the learned space is composed of a predefined probabilistic distribution for every input, instead of values, in order to address the problem with a non-regularized latent space. Because most of the objects in the real world are discrete, the Vector Quantised Variational AutoEncoder (VQVAE) version uses a discrete set of values for the latent space representation.

The advantages of proposed work over the existing body of connected literature thus stem from several novel mechanisms. First, the paper presents a fresh, independent approach to SR, as compared to traditional single and hybridized LCF. Second, the procedure offers a more effective way to handle noise, superimposed spectral lines, as well as variability and non-stationarity in signals. Finally, an embedded AE in three variants is used to compress the signal and a new loss function to integrate all six SR modes is adopted.

3. Problem statement

The most studied information about SR considers the central frequency values and their corresponding intensity values in the frequency spectrum. Several methods have been proposed to reduce signal noise and extract these features from the signal. The main problem is not only the extremely low intensity of the electromagnetic field, but also the high intrinsic variability of the SR signal.

It is widely considered that the LCF is the most convenient algorithm to extract these parameters (Price, 2016). Its application in SR was first proposed in (Sentman, 1987) (Eq. (1)):

$$L(t) = \sum_{i=1}^{i=n} \left(\frac{Amplitude_i}{1 + \left(\frac{(t - Center_i)}{Width_i} \right)^2} \right) \tag{1}$$

where $L(t)$ represents the sum of the Lorentzian curves, $Amplitude_i$ stands for the highest value of each Lorentzian peak, $Center_i$ is the offset between zero and the center of each Lorentzian peak and $Width_i$ represents the range of the peak.

The LCF algorithm is a nonlinear curve fitting method that involves adjusting a sum of multiple Lorentzian functions to the SR spectrum. Specifically, as shown in Eq. (1), the method fits the sum of six Lorentzian curves, each representing one of the SR modes. This approach inherently accounts for the nonlinear nature of the signal by simultaneously adjusting the parameters of all six Lorentzian peaks to best fit the observed data.

In our study, we propose to design an AE to learn the underlying behavior of the SR signals from clear registers and apply this learned pattern to enhance non-ideal, noisy registers. To improve the ability of the model to extract the Lorentzian peaks present in SR signals, we incorporate a regression layer into the AE architecture. This additional layer enriches the latent representation by explicitly encoding information related to the peak characteristics, improving the model's capacity to reconstruct the signals and accurately capture important resonance features.

The loss function used during training combines reconstruction and regression losses. The reconstruction loss, calculated using the average squared difference, ensures an accurate reproduction of the input signal, effectively denoising it. The regression loss penalizes deviations in the predicted Lorentzian peak parameters, guiding the model to robustly extract these specific resonance features. This combined loss function enables the model to denoise the signal while retaining critical resonance information.

Rather than integrating directly with the traditional LCF algorithm, our DL model serves as an alternative. The AE learns to reconstruct the resonance modes without explicitly fitting Lorentzian curves, addressing the difficulties faced by LCF in handling weak and noisy signals. This approach provides a more robust means of analyzing SR data, especially in scenarios where traditional fitting methods struggle due to high noise levels or the presence of multiple overlapping modes.

We use high-quality, low-noise SR data to train and evaluate the performance of the proposed DL model. As will be shown in Section 4, the data set is prepared following established procedures, applying the preprocessing pipeline associated with each measurement station and adapting it to the model requirements, such as scaling and fixing dimensions. This approach ensures that the data set adequately represents the diversity of SR patterns necessary for effective training.

The model is calibrated using an automatic hyperparameter tuning optimizer. Various architectures and configurations are compared to identify the most successful. Alternative loss functions are considered during the optimization process, to establish the one that enhances model performance. The finally obtained values are given in Section 4.

To clarify the logical flow of this contribution, Fig. 1 condenses the complete processing chain into six conceptual steps. First, the **raw SR signal** register delivers a 256-point frequency register vector (red frame). Second, the **convolutional encoder** (green left funnel) compresses the 256-D frequency register to a *10-dimensional* latent vector. Third, in the **latent bottleneck**, the central block shows that the same encoder–decoder skeleton can host a plain AE, a VAE, or a VQVAE. Fourth, the **convolutional decoder** (green right funnel) inflates the latent vector back to a 256-D spectrum. Two mutually exclusive heads are shown: **Lorentz reconstruction** (blue frame), which is used when the network is trained to reproduce a perfectly denoised Lorentzian fit (ideal for learning peak geometry) and **raw reconstruction** (red frame) that lets the network learn a noise-tolerant auto-encoding directly in the measurement space. Fifth, the **frequency-regression branch** (yellow diamond) taps the latent space with a fully connected head that simultaneously regresses the six mode centers $\{f_1, \ldots, f_6\}$. This term sets a second objective in the loss function Eq. (2), forcing the bottleneck to keep physically meaningful information. Eventually, **sample selection** (bottom left) illustrates the training sets: the 70 % clearest segments train the autoencoder, where the frequency values are correctly extracted using the LCF, while the remaining 30 % noisy spectra are considered to test the generalization of the model.

Altogether, the diagram shows explicitly how the proposed architecture *encodes* even heavily corrupted spectra into a compact physics-aware latent space, how either a pristine Lorentzian profile or the best possible cleaned version of the raw data is *reconstructed* and how *regression* takes place for all six resonance frequencies in a single forward pass.

4. Materials and methods

The proposed methodology is based on the use of an AE to reconstruct the original signal, while decreasing its variability by dimensionality reduction in a learned space. The original AE architecture has been modified to reinforce the process of extracting the central SR modes. The

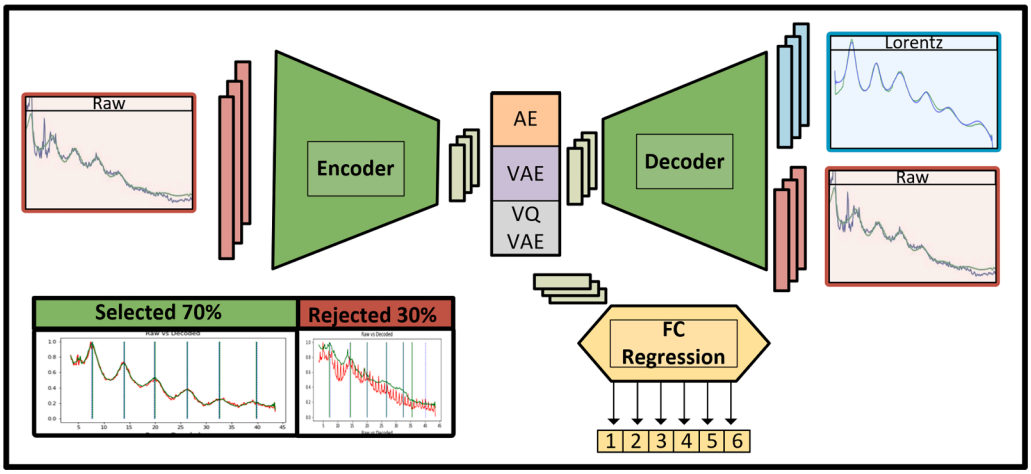

Fig. 1. End-to-end workflow of the proposed hybrid deep–learning solution for SR encoding analysis.

methodology uses the ELF low-noise registers as the training data set. In these registers, the LCF has been demonstrated to be an almost perfect representation of the SR signal. Therefore, the central frequency values and the LCF are considered ground truth for training purposes. The hyperparameters are obtained by an automatic tool, and all the inputs are normalized.

This research is based on the study of six different approaches for implementing a modified AE methodology. The input of the network is common for all the six versions, which is the raw input. For the output, two different strategies have been performed: the first is the classical AE, with the raw SR spectrum; the second is the usage of the LCF for reconstructing the signal.

4.1. Architecture

A diagram of the general architecture can be seen in Fig. 2. Its flow can be described algorithmically through the following steps. On the left side, the raw input, common for all variations in this research, composed of 256 values, is passed to a CNN encoder, which leads to a recognition of the different shapes in the signal. The CNN encoder is then made up of three hidden layers. The first reduces the input to a vector of 128 components with 16 channels; the next reduces the length to 64 components and increases the number of channels to 32; the last convolutional layer reduces the length to 32 components and increases the number of channels to 64. The output of the last convolutional layer is flattened to 2048 units (32-component vector with 64 channels). The upcoming central stage is the learned space, with a fully connected layer that is linked to the learned previous layer and another dense one which is connected with the decoder. The learned space is composed of 10 units. Three different AE architectures are evaluated to explore a variation of the performance with distinct behaviors. The right part of the diagram subsequently displays the decoder. This part is just the complementary model of the encoder. It takes the learned space vector to reconstruct to 64 channels of 32 positions and decode a 256-length vector through three CNN layers. The right layer depends on the architecture, as explained before: Raw for reconstructing or Lorentz to allow more flexibility. Finally, on the bottom part of the figure it can be seen that this methodology adds a deep regression part in order to take into consideration the central frequency values from the LCF. The aim is to force the learned space to represent the central frequency modes. This part is composed of three layers, first the input one, the hidden layer with 128 neurons, and the output layer with six neurons, one for each SR mode present in the SR registers.

The learning algorithm consists of minimizing the loss function associated with each of the three architectures: AE, VAE, VQVAE. The three designs have within their loss function the $L_{reconstruct}$ and L_{freq}, although the specific implementation depends on the nature of the architecture. The former is related to the Root Mean Squared Error (RMSE) between the expected output and the decoder output, whereas the latter is the added regression loss, calculated following Eq. (2), where f_i stands for the Lorentz-extracted frequency, $\overline{f_i}$ is the decoded frequency value and $\hat{f}_i$ is the averaged value of the central frequency associated to each SR mode. This term is included in order to normalize the importance of the six components. k is the weight for the loss, in order to obey the same value interval. For the sake of clarity, the SR mode can be seen as a small peak with a bandwidth, a peak intensity value and a central frequency. In this case, we are interested in estimating just the central peak value.

$$L_{freq} = k \cdot \sum_{i=1}^{6} \left(\frac{f_i - \hat{f}_i}{\overline{f_i}} \right) \tag{2}$$

The complete loss functions for the three DL models are:

(A) **AE:** standard loss function with the aggregated regression loss term - $L_{AE} = L_{reconstruct} + L_{freq}$.
(B) **VAE:** add the Kullback–Leibler divergence as $L_{regularizing}$, such that the latent space is distributed continuously, and penalize when not normal distribution.
(C) **VQVAE:** add the L_{cb}, to get the chosen codebook vector as close to the encoder output as possible, and the Lsg (stop gradient), to force the encoder output to commit to its closest codebook vector as much as possible. A full explanation of this can be found in Wu and Flierl (2020).

To provide a mechanism for denoising the signal, we have presented possible alternatives for the output: to reconstruct the decoded output from the original raw SR signal **(1)** or to reconstruct it using the estimate LCF **(2)** (Fig. 2). The LCF has the advantage of allowing the model to learn from a perfectly denoised representation, but could lead to overfitting.

4.2. Data

The SR data were obtained from our station located in Sierra de Filabres (Lat. 37.1, Long −2.6), province of Almería (Spain) (Cano-Domingo et al., 2021; Gázquez Parra et al., 2015). The observatory can capture the two orthogonal magnetic fields; however, only the NS is considered, such as to ensure the homogeneity of the data. The samples were collected over five years, from the 1st of January 2016 to the 31st of December 2020. The final amount of SR registers is 79281. The data comprise the raw signal, the LCF, and the extracted central frequency value for each SR mode.

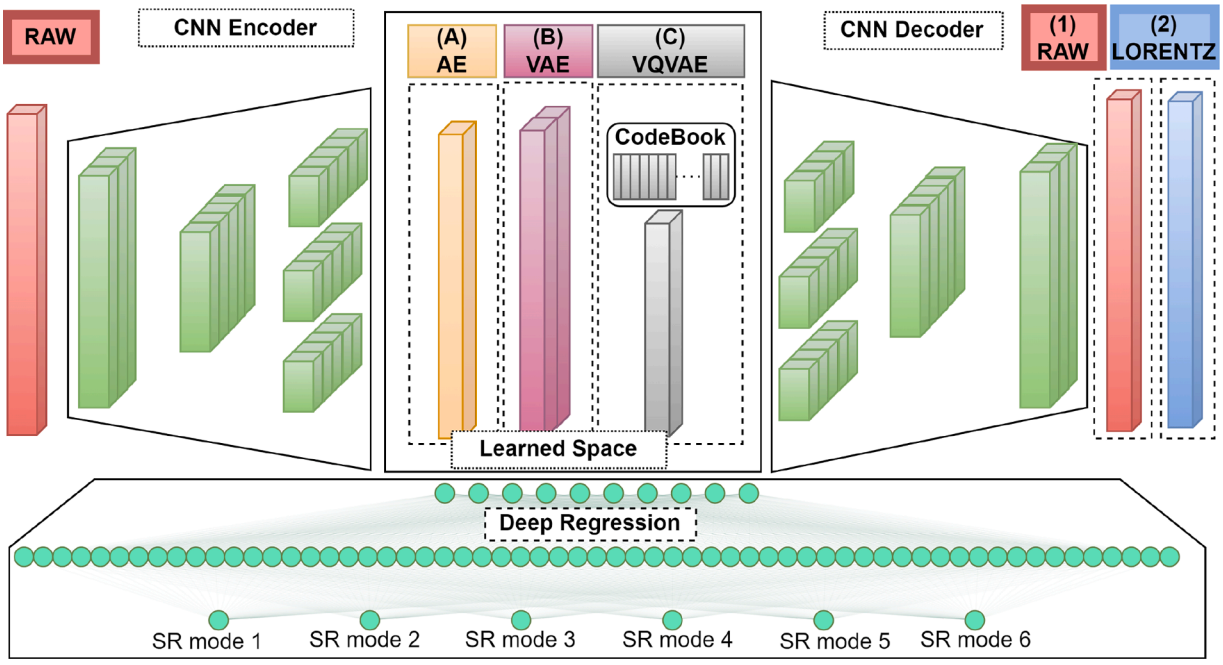

Fig. 2. General model of the DL methodology used in this study. Different AE versions are used to compare its performance: **(A)** AE, **(B)** VAE, **(C)** or VQVAE. The output can be: **(1)** Raw signal or **(2)** Lorentz signal.

Two processes have been employed to select the data set. First, we use a reject filter presented in the previously commented research (Cano-Domingo et al., 2021) and also a variability metric focused on the frequencies between 6 Hz and 42 Hz. Second, the data are organized in three different groups. For training purposes, the best-labeled set is chosen. It means taking the registers not rejected by the filter and the ones with Lorentz performance higher than 90 %, leading to 40,671 inputs. The second group is used for validation, consisting of the rejected registers. The rejected register group is made up of 34,090 inputs. The last group consists of all the SR input available, to analyze an overall performance. Therefore, the total number of inputs is 79,281.

4.3. Computational and algorithmic complexity

Our framework heavily relies on convolution-based encoders and decoders, as implemented in our three architectures (AE, VAE, and VQVAE). Most of the computational cost arises from these convolutional operations. Specifically, for a one-dimensional input signal of length $N = 256$ that passes through three convolutional layers (each approximately halving the spatial dimension by using a stride of 2), the complexity per convolutional layer can be expressed in terms of FLOPS (Floating-Point Operations) as in Eq. (3):

$$\text{FLOPS}_{conv} \approx 2 \times C_{in} \times C_{out} \times K \times \frac{N}{S}, \tag{3}$$

where C_{in} and C_{out} represent the input and output channels, K is the kernel size, N is the length of the input, and S is the stride used. The factor 2 accounts for multiplications and additions per convolution. In our configuration, we use three convolutional layers with moderate channel expansions: from 1 to 16, from 16 to 32, and from 32 to 64 channels. With strides of 2, the computational complexity remains manageable, typically resulting in millions of FLOPS per forward pass, comfortably handled by modern GPUs. For the **VQ-VAE**, an additional complexity arises from the vector quantization step, involving the calculation of pairwise distances between encoder outputs and embedding vectors. This complexity is given by Eq. (4):

$$\text{FLOPS}_{vq} \approx 2 \times (\text{batch\_size} \times L \times D \times E), \tag{4}$$

where L is the latent spatial dimension after convolution, D is the embedding dimension ($16 \leq D \leq 64$), and E is the number of embeddings ($128 \leq E \leq 512$). Again, these values are selected to keep computational overhead within feasible limits. In the case of the **VAE**, the latent sampling operation (reparameterization trick) involves negligible overhead compared to convolutions, being primarily composed of simple element-wise operations (Eq. (5)):

$$\text{FLOPS}_{vae\_sampling} \approx O(\text{batch\_size} \times \text{latent\_dim}). \tag{5}$$

Overall, the primary computational load is driven by convolutional operations, typically resulting in a total complexity of tens to hundreds of millions of FLOPS per forward pass, depending on precise network hyperparameters. With current GPU hardware capable of achieving TFLOPS (trillions of FLOPS), the proposed models allow efficient training and inference, even for large-scale deployments.

5. Results

In this section, we present a set of results to show the performance of our algorithm. First, three particular cases are presented as a representation of the DL performance over a SR register with different levels of noise. Subsequently, a brief comparison between the RMSE for every DL model is conducted. The next part analyses the frequency mode distribution of the LCF and also for each of the DL algorithms. A special mention will be made to a quantitative likelihood analysis between the selected and non-selected registers. Finally, a comparison between the diurnal SR patterns obtained from two DL models and the LCF is discussed. A detailed description of the experiments can be found at the public Git repository: https://github.com/carloscanodomingo/SR_encoder

5.1. Outcome

In Fig. 3, three SR registers used by the six DL models can be seen. For the sake of comprehensibility, we have separated the three DL models which use the Lorentz signal as output, in the top row, from the other three that use the Raw one, in the bottom row.

The left column represents a SR register with low noise. In this case, the Lorentz function can fit the signal entirely, and also, the DL Lorentz

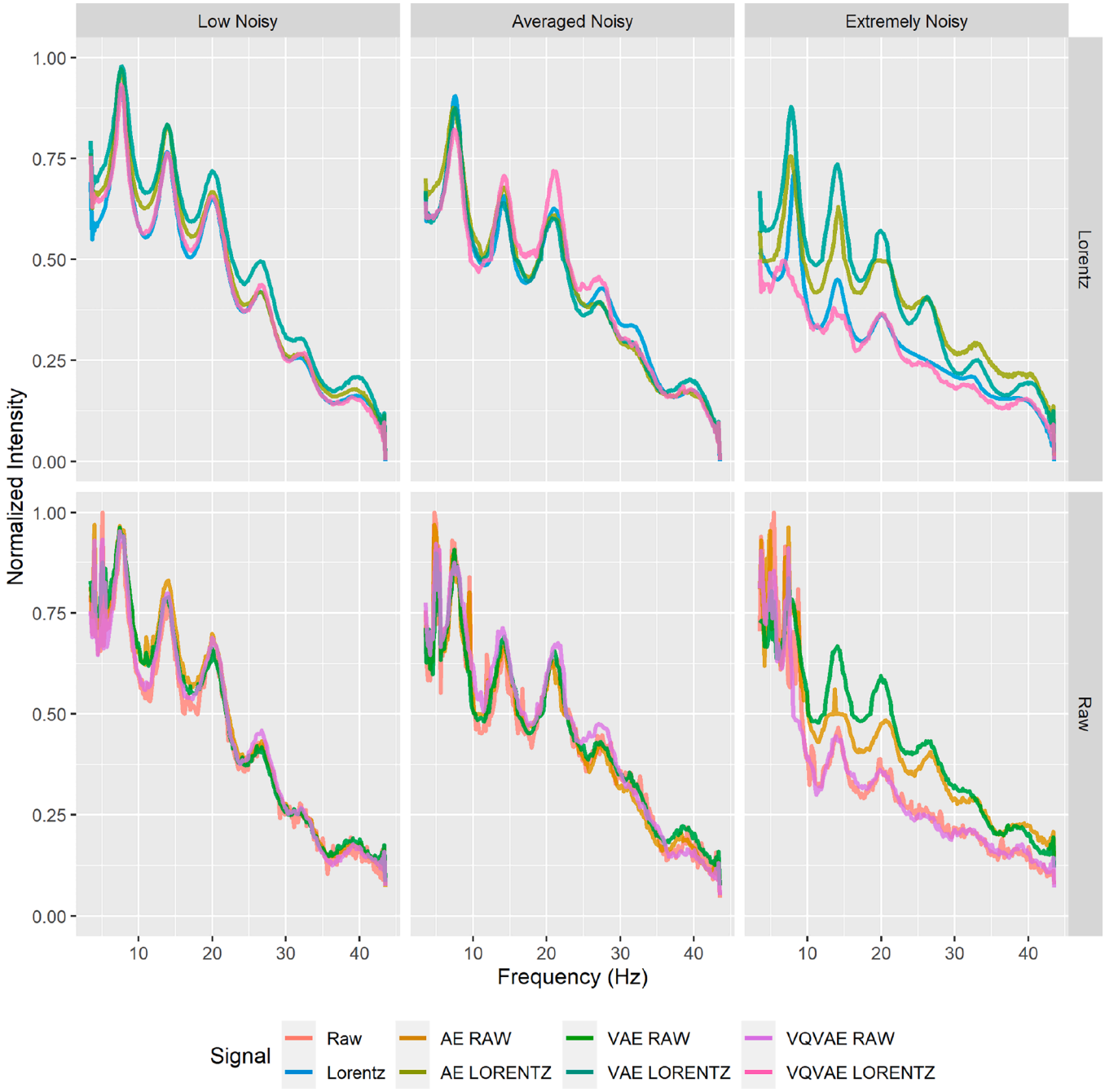

Fig. 3. SR frequency spectrum for not noisy register (left), average noisy register (central), extremely noisy register (right).

methods perform in a very similar way in terms of the position of the peaks. Equivalently, when it comes to the raw DL models, the positions of the peaks are also very similar to the ones of the original signal. The central column shows an additional standard SR register, with a substantial level of noise, but the result of the LCF fulfils the required performance. Although the Lorentz DL models show slight differences between the three reconstruction signals, it is seen that the peaks are located very close to the LCF ones. It can be noticed that the main discrepancy is found with the VQVAE Lorentz model. The raw DL models also show a compelling performance. It is possible to see that the 10 Hz noisy peak in the input is ignored by the three models in the decoded signal. Furthermore, most of the noise contained in the input signal is not present in the output. This effect is possibly due to the dimensionality reduction performed within the learned space layer, as the system leaves the noise variability out from the encoding. It may be observed that the VQVAE model fit performance is substantially lower than that of the other two models. The 5th mode also shows higher error than the rest. However, this effect is also noticeable using the Lorentz process. The right column shows an extremely noisy SR register. One can observe that the noise level makes it exceedingly difficult in this case to fit a Lorentz curve. As mentioned previously, the fitting mathematical procedure misestimates the SR signal completely. Not only the first mode has been incorrectly located very close to 10 Hz but also the 4th SR mode has not even been identified. The result for the DL models shows noteworthy improvements over the LCF. The three can locate the six peaks, and the decoded signal is more plausible than in the LCF. It is possible to observe that the VAE performs considerably better than the rest, remarkably similar to a SR register with no noise. On the con-

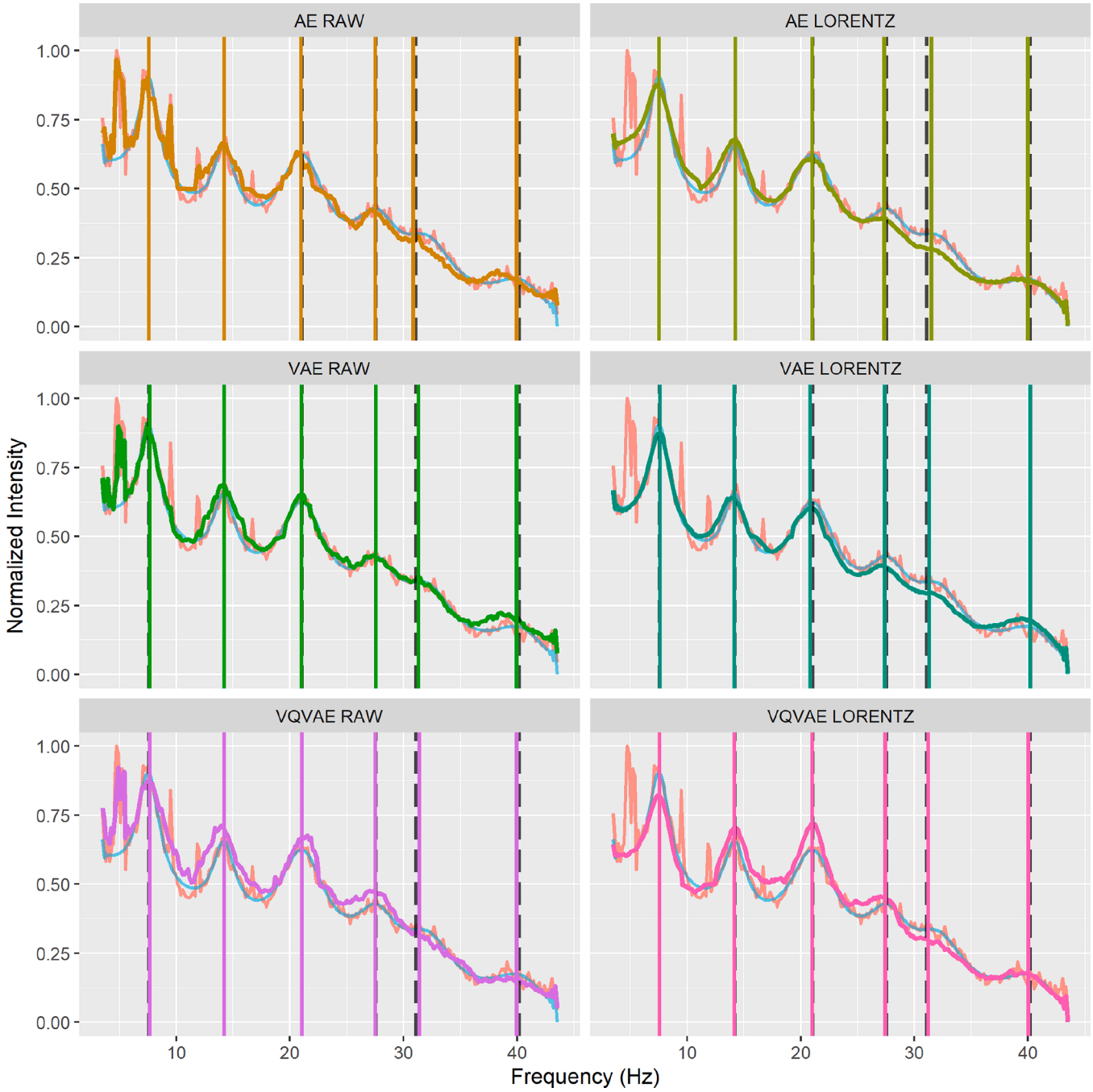

Fig. 4. Frequency and decoded signal DL output for an average noisy register. Black lines: frequency extracted by the LCF.

trary, the VQVAE Lorentz shows a very irregular pattern. Apart from the VQVAE, the raw DL models have encouraging results. Both the VAE and AE can reduce the noise level of the original signal and reconstruct a more likely SR register than the LCF. Although the peaks in the raw signal are barely discernible, excluding the first mode reveals a consistent pattern between this signal and the two aforementioned DL models. The results show very similar behavior to the LCF when the noise level is not exceptionally high. On the other hand, when the noise level is relevant enough, the DL algorithms provide a noticeable improvement over the fitting procedure. A clear conclusion that emerges is that, considering that a strong level of noise is present in around 40 % of our SR registers, the employment of the DL methods becomes very relevant.

The frequency estimated for the average noisy register along with the decoded signal of each of the DL models can be observed in Fig. 4. The frequency result is also present in Table 1. It can be seen that there are no substantial differences between the six SR modes with respect to the reference value (in the corresponding column). These results are consistent with the DL methodology presented. A substantial amount

Table 1
Frequency summary of the six DL models applied to an average noisy register and LCF as the reference.

		RAW			LORENTZ		
	LCF	AE	VAE	VQVAE	AE	VAE	VQVAE
SR 1	7.55	7.6	7.67	7.65	7.52	7.61	7.56
SR 2	14.20	14.2	14.21	14.22	14.23	14.17	14.18
SR 3	21.05	21.0	21.00	21.06	20.99	20.83	21.00
SR 4	27.55	27.5	27.58	27.53	27.36	27.39	27.44
SR 5	31.05	30.9	31.29	31.38	31.52	31.31	31.21
SR 6	40.15	40.0	39.95	39.97	40.00	40.22	40.03

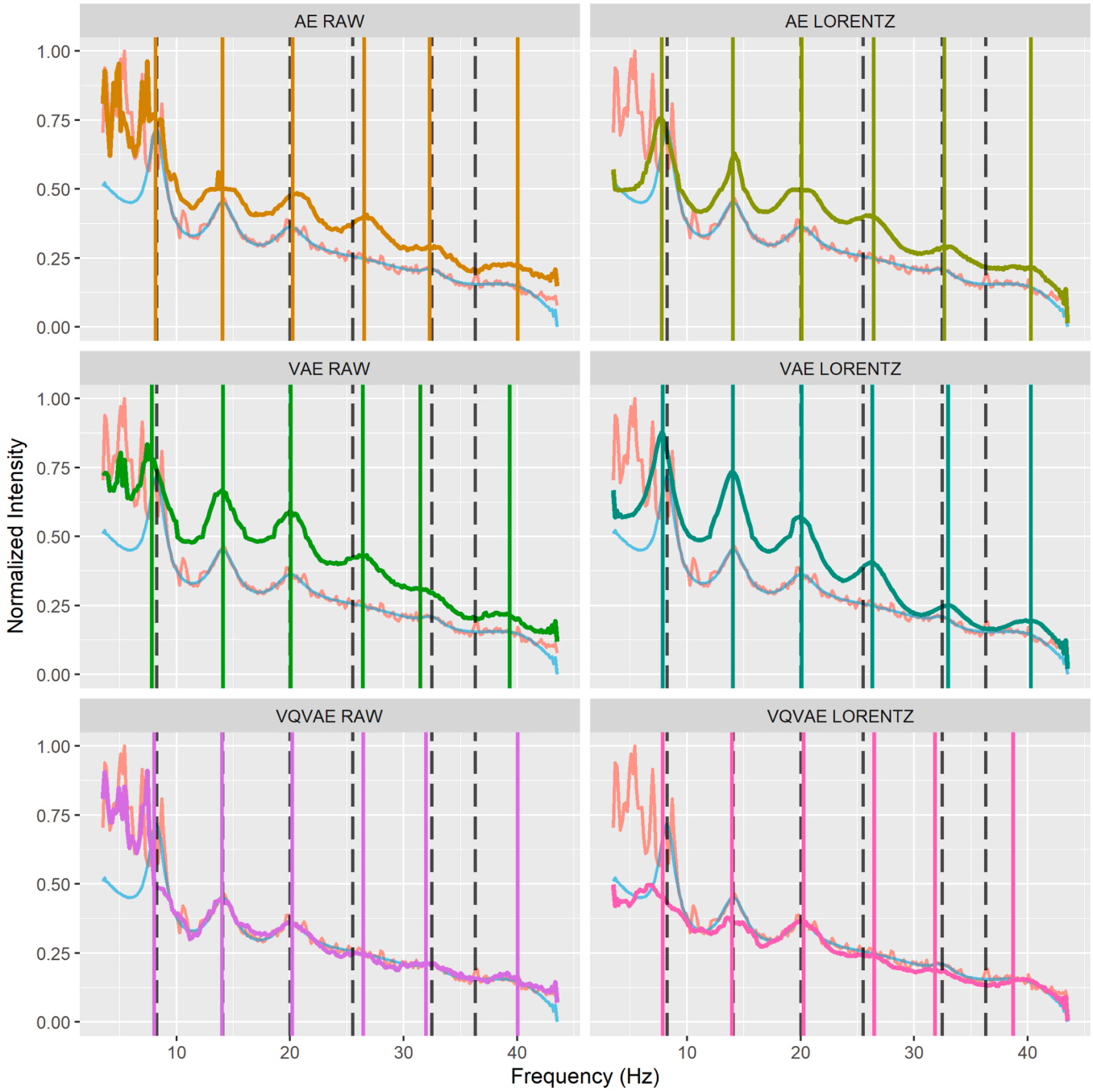

Fig. 5. Frequency and decoded signal DL output for an extremely noisy register. Black lines: LCF extracted frequency.

of average noisy SR registers is present in the input data set. Therefore, the DL algorithm has effectively learned to extract the frequency even in the presence of considerable noise, producing results that closely match those obtained by the Lorentz algorithm. Since the Lorentz algorithm provides values that accurately represent the true characteristics of the SR, this close match indicates that the DL outputs are also a true representation of the real nature of the SR.

A completely different behavior can be seen in Fig. 5. In this case, the noise level is extremely high compared to the signal. It is important to mention the level of noise around the 1st SR mode and the low level of the signal in the peaks associated with the 4th and 5th modes. Table 2 shows the estimated and reference frequencies. In the first mode, the LCF captures a value of 8.25 Hz, which seems considerably far from the typical results obtained in our observatory. At the same time, almost all the DL models extract a value closer to the usual register and are also consistent with the visual inspection of the raw data. The 2nd and 3rd SR modes are almost equal along DL models and LCF. The behavior of the 4th mode is completely different. There is a considerable consen-

Table 2
Frequency summary of the six DL models applied to an extremely noisy register and LCF as the reference.

		RAW			LORENTZ		
	LCF	AE	VAE	VQVAE	AE	VAE	VQVAE
SR 1	8.25	8.17	7.82	8.04	7.77	7.85	7.89
SR 2	14.05	14.04	14.08	13.99	14.04	14.05	13.95
SR 3	20.00	20.21	20.08	20.18	20.12	20.09	20.27
SR 4	25.50	26.54	26.42	26.47	26.44	26.32	26.49
SR 5	32.45	32.31	31.49	31.97	32.66	32.99	31.83
SR 6	36.30	40.05	39.33	40.02	40.28	40.30	38.72

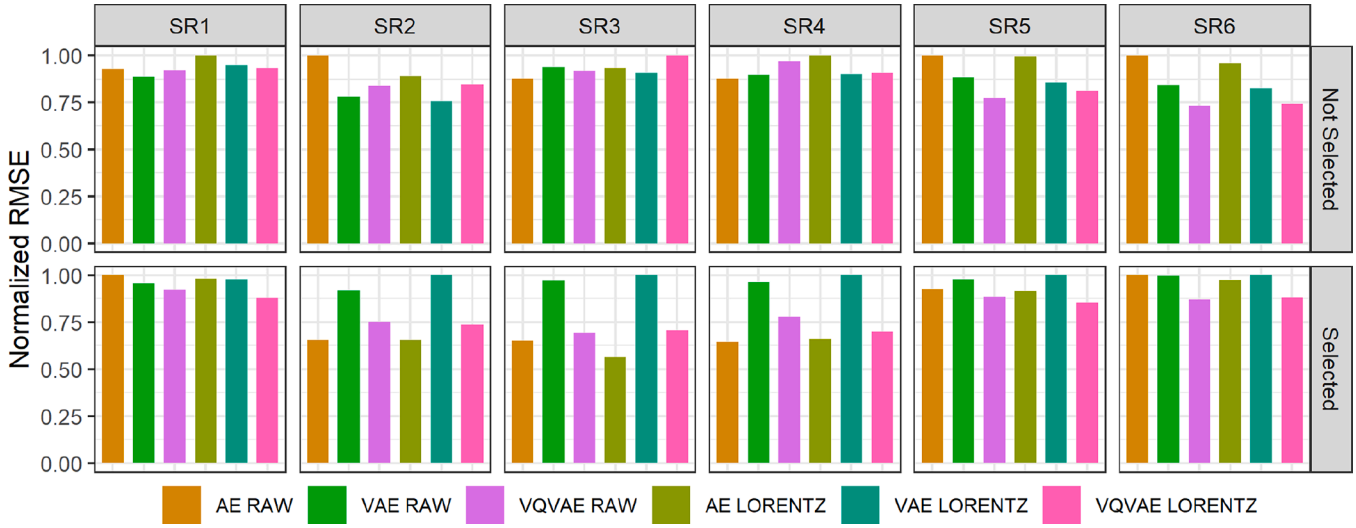

Fig. 6. RMSE normalized by the maximum value of each mode and type. Selected refers to the registers that present good condition to perform a LCF procedure.

sus between the DL methods, with slight differences among them; all are around 26.5 Hz. However, the LCF has extracted a value of 25.50 Hz, which is not correct in light of the typical values of the 4th mode and also from the visual observation of the raw signal. It can be explained by the fact that the raw signal has a strong level of noise around the 25 Hz and the peaks are almost indiscernible, so that any noisy little peak can be considered as the LCF peak by the fit procedure. The 5th mode does not show substantial differences either with the LCF or among the DL models, due to the prominence of this peak in the raw signal. On the other hand, the 6th mode presents a typical problem using a fit procedure; the RMSE is not taken into account properly because of the relatively low value of the signal in this part. The fit algorithm has chosen a value that minimizes the overall error, but not this mode. The LCF extracts a frequency of 36.30 Hz while the DL models are around 40 Hz. The Lorentz value is utterly inaccurate, as can be seen in the raw signal, but the DL method can obtain a very plausible SR decoded segment, even in this 6th SR mode.

5.2. Interpretation

In view of the above results for the six SR modes, it is crucial to notice that the decoded values of the AE and VAE are considerably higher than those present in the raw signal. In contrast, the VQVAE model follows the raw signal almost perfectly. Another important insight of this result is the capability of the DL models to improve the LCF extraction procedure. Even if the six models have different approaches to reconstructing and estimating the peak frequencies, there are promising outcomes in all of them.

With respect to the RMSE of each architecture, Fig. 6 shows the differences between the estimated central frequency value extracted by the LCF and the frequency output of the DL models. It is possible to observe that the VAE and VQVAE perform better when the noise level is considerable. In the bottom row of Fig. 6, the result for the Selected Registers is shown. In general, it can be seen that the VAE models obtain higher RMSE than the rest, which could be motivated by the randomization of the latent space that can be seen as a generalization. It can be noticed that the AE algorithm gets the best results for the 2nd, 3rd and 4th and the VQVAE in the rest of the modes. This can be explained by the fact that the 2nd, 3rd and 4th are usually prominence peaks, while the others often have a high part of the noise, which can be a sign of the lack of generalization for AE. This hypothesis is also supported by the RMSE in the top row. In this row (non-selected patterns), the AE algorithm performs worse than the rest of the DL models. Strikingly, the result for the VAE Raw shows the best performance in several modes, and this is especially relevant for the first mode. As it happens for the Selected registers, the VQVAE shows the best results in the 5th and 6th modes. It is important to remark that the RMSE values for the non-selected registers cannot be considered as a reference, but can be seen as a good indicator.

In order to evaluate the accuracy of the DL methodology, we have summarized the frequency distribution of the six SR modes using the LCF (Fig. 7). For each SR mode, the two distributions are represented together. The distributions for all registers (selected and non-selected) are plotted in the outer area and with a strong color, while the distributions for only the selected ones are plotted in the inner area with a lighter color. In line with the earlier results, the 1st, 5th and 6th modes present a non-realistic pattern, completely unrelated to the selected ones. The other modes do not show this great divergence, due to the previously mentioned prominence of these peaks. The effect of the most relevant criterion for rejecting a SR register can be seen in the 1st mode: All registers with an extracted 1st mode value outside the interval 7.5 Hz and 8.2 Hz are not previously considered as valid SR registers.

In the following, we have evaluated quantitatively the similarity between the LCF for selected registers and the estimation for all registers using the DL models by using the Kolmogorov-Smirnov (KS) test (Berger & Zhou, 2014), where lower values represent a more likely common origin. This test measures if two samples could have been obtained from the same distribution. For each mode, the LCF frequency in the selected segments has been tested with the estimated output frequency of the DL model considering all the registers. The results are summarized in Table 3. The reference column represents the KS test between the LCF output for all segments and the fit for the selected registers, which can be considered as its performance.

A general improvement appears when using the DL models, particularly relevant for the 1st mode, where all perform better than the LCF. DL Raw models get a KS value around 0.08, substantially lower than the DL Lorentz models with 0.11. Both are much better than the result using the LCF, with a value of 0.22. This can also be observed through

Table 3
KS results for each DL model and SR mode.

		RAW			LORENTZ		
	Ref.	AE	VAE	VQVAE	AE	VAE	VQVAE
SR1	0.220	0.080	0.079	0.086	0.100	0.094	0.128
SR2	0.096	0.085	0.058	0.081	0.094	0.100	0.080
SR3	0.039	0.075	0.058	0.059	0.048	0.054	0.056
SR4	0.071	0.046	0.046	0.096	0.044	0.056	0.055
SR5	0.066	0.040	0.040	0.035	0.041	0.037	0.039
SR6	0.075	0.056	0.066	0.050	0.078	0.085	0.063

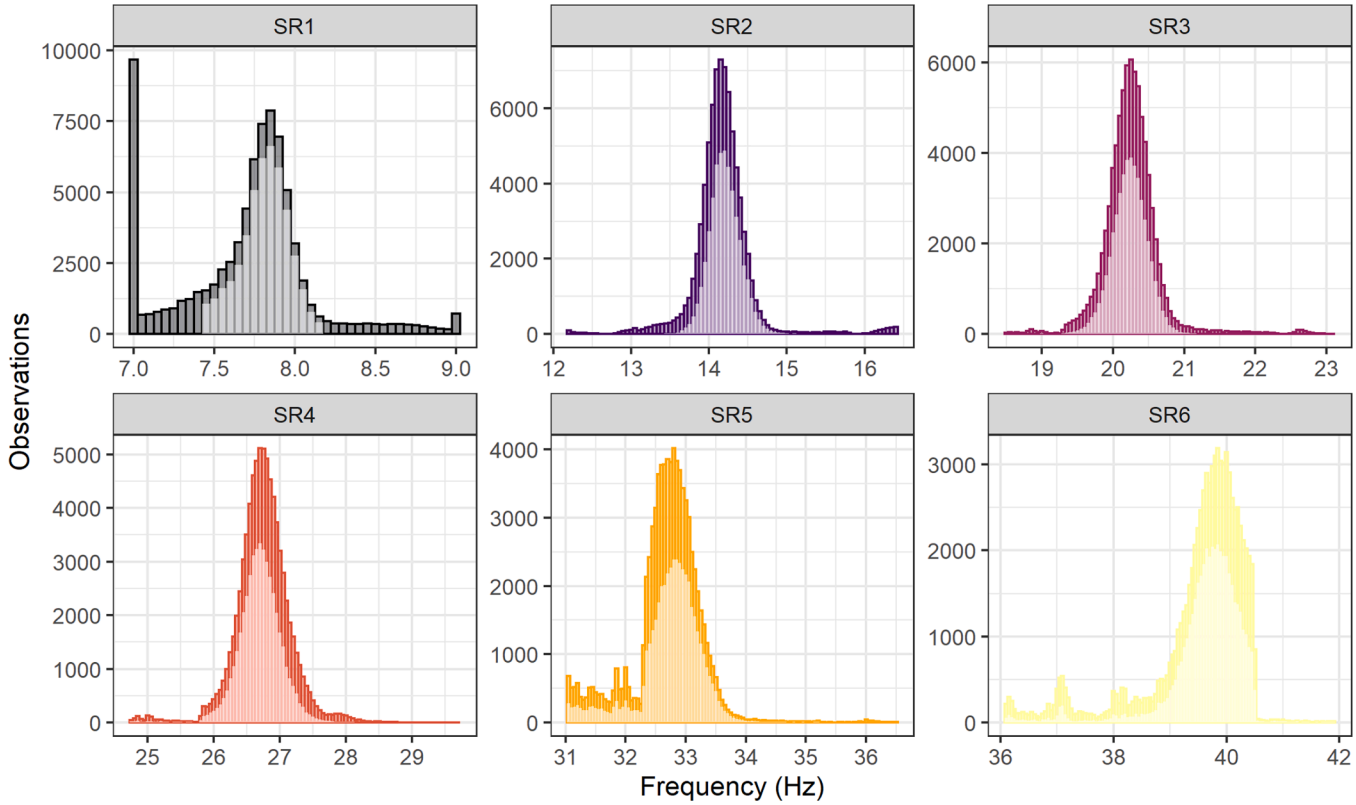

Fig. 7. Frequency distribution of the six SR modes by the LCF: all registers in the outer area with darker color, the selected ones in the inner zone with brighter color.

the frequency distribution in Fig. 8(a). A fit curve has been included to help with the comparison among the DL models. This curve is the best Skew Normal Distribution (SND) fit to the selected LCF frequency values. Compared to the LCF, the frequency distribution of the DL models is completely different for the non-selected, but very similar for the selected ones.

The DL models applied for the 2nd, 4th, 5th and 6th modes perform substantially better than the LCF. Commonly, for all modes, the VAE Raw model obtains the best results. Surprisingly, no signs of improvement were found for the 3rd SR mode. The frequency distribution of each DL model can be seen in Fig. 8(b). As it can be deduced from the figure, there are no relevant differences between the models, and also, the data adjust almost entirely to a SND. It is also important to mention that the value is considerably lower than for the rest of the modes in the LCF column. The reason for this somewhat contradictory result is not completely clear. However, two effects could explain it: one is the less affected by noise lowest part of the spectrum, near 0 Hz, present in most of the non-selected registers. Secondly, the magnetic field intensity decreases with the frequency in our experimental data, but it is still high enough around 20 Hz, sometimes even higher than the magnetic field intensity in the 2nd mode.

This result clearly shows that the critical error between the selected registers and the non-selected ones using the LCF is located in the 1st mode. However, by using the DL algorithm, the similitude between the frequency values in the selected and non-selected registers can be drastically reduced. It is essential to emphasize the importance of having a processing tool that does not reject any of the SR registers.

Diurnal variations on SR frequency is a commonly studied event in SR research. In this pattern, the frequency value is averaged for each hour of the day. The regular differences among these 24-h evolutions in different seasons are also well established. For validation, we included the diurnal variation separated by season for all modes, Fig. 9.

For comparison purposes, we have chosen the two most promising DL models, VAE Raw and VQVAE Lorentz, and the LCF. The frequency values are separated by selected and non-selected registers. For all the modes, the LCF in the selected registers performs outstandingly, with very similar results to those obtained by other observatories presented in the commented bibliography. It can also be observed that the three models behave in an almost identical way in the selected rows - it is hard to distinguish the lines between them.

In Fig. 9(a), the frequency diurnal variation of the first three modes can be observed. For the 1st mode, it can be seen that the differences between the selected and non-selected ones using the LCF are significant. The selected are comprised in the interval (7.6–7.85), while the non-selected expand the range to the interval (7.15–7.85). This lower value cannot be plausible considering the results of other observatories. The diurnal pattern obtained by the DL models shows a more likely variation, not only in terms of a more reduced interval, but also the shape of the pattern is almost identical to the selected LCF, one for each season. Although the two DL models show clear improvements, the VAE Raw achieves a better resemblance with the selected pattern. For the 2nd mode, the values are closer between the selected and non-selected registers. Nonetheless, the DL models obtain a more similar interval than the LCF between the selected and non-selected registers. As noted in the previous results, the 3rd mode characteristic allows the LCF to achieve satisfactory outcomes even when the level of noise is relatively high. Therefore, the results are very similar between the selected and non-selected SR registers. The major improvement using the DL model can be found focusing on the winter season. In this season, the values of the LCF are in the interval 20 Hz to 20.45 Hz, whereas, in the non-selected registers, the values are from 20 Hz to 20.35 Hz. This difference is also followed by the VAE RAW model. Surprisingly, the VQVAE model constrains their variation to 20 Hz to 20.35 Hz as in that of the selected.

The 4th, 5th and 6th frequency diurnal variation can be found in Fig. 9(b). It can be observed for the 4th and 5th mode that the major differences between the LCF and the DL models are found in the winter period. In this season, the values from the DL models seem to be more in line with the rest of the year, whereas the LCF has a sharp difference

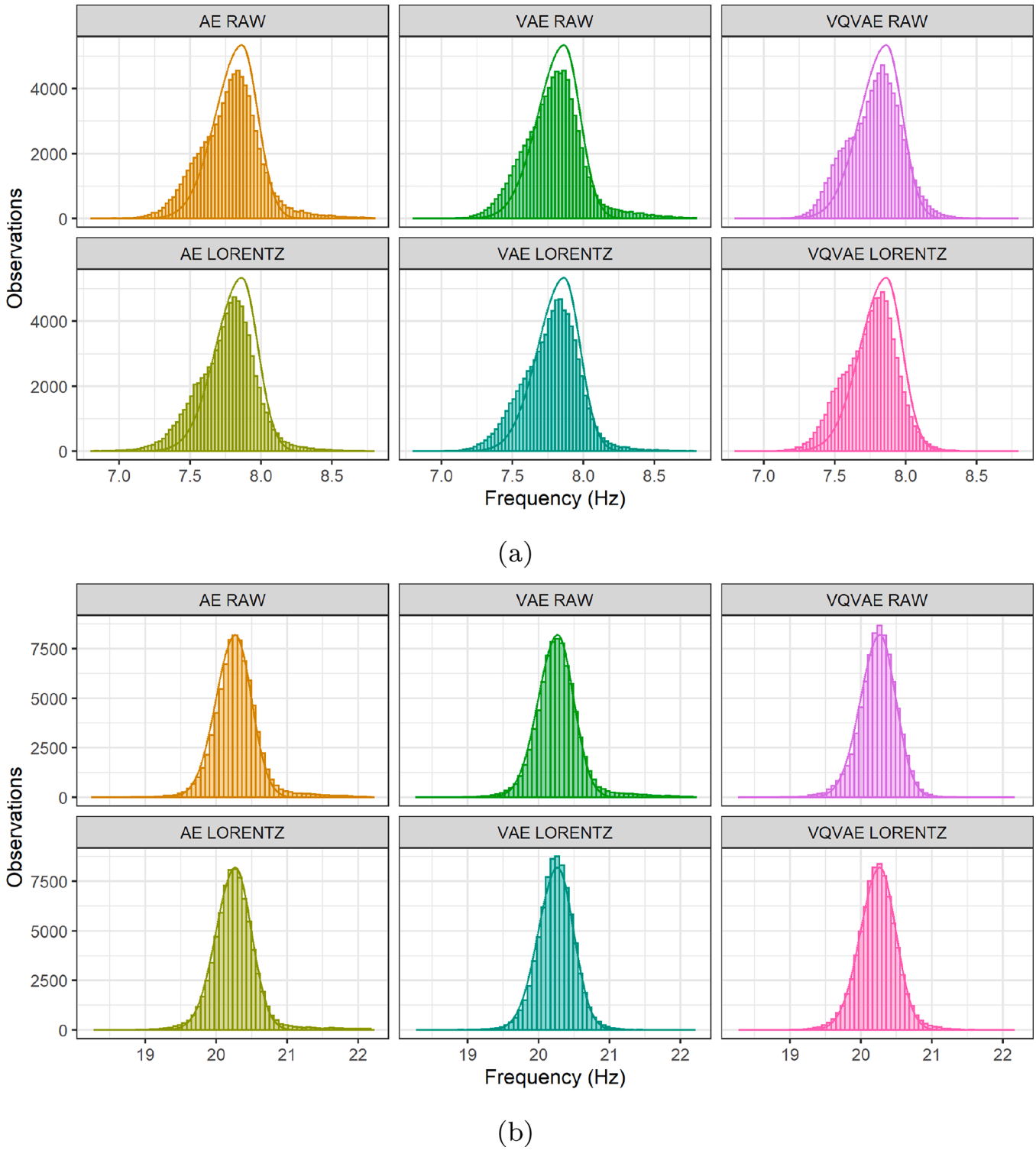

Fig. 8. Best SND fit to the selected LCF frequency values versus DL output. **(a)** 1st SR mode, **(b)** 3rd SR mode.

from the previous and following season. For the 6th mode, the results have to be taken cautiously due to two effects: the high level of noise produced by the power lines and also due to the low level of magnetic intensity in that frequency band. Nevertheless, the DL models perform in a very similar way to the LCF. The most striking observation that emerges from this mode is that, despite the problems involved, the system can show substantially more minor differences between the selected registers and the non-selected ones than the LCF.

6. Comparison to direct deep learning signal processing

To assess the effectiveness of our VAE–based algorithm beyond simple frequency prediction, we also compare it against a pure DL approach that uses a CNN for frequency estimation. Unlike our proposed AE approach, which simultaneously learns to encode the signal and reconstruct it, the CNN model focuses exclusively on predicting frequency from the input signals. This comparison highlights the advantage of

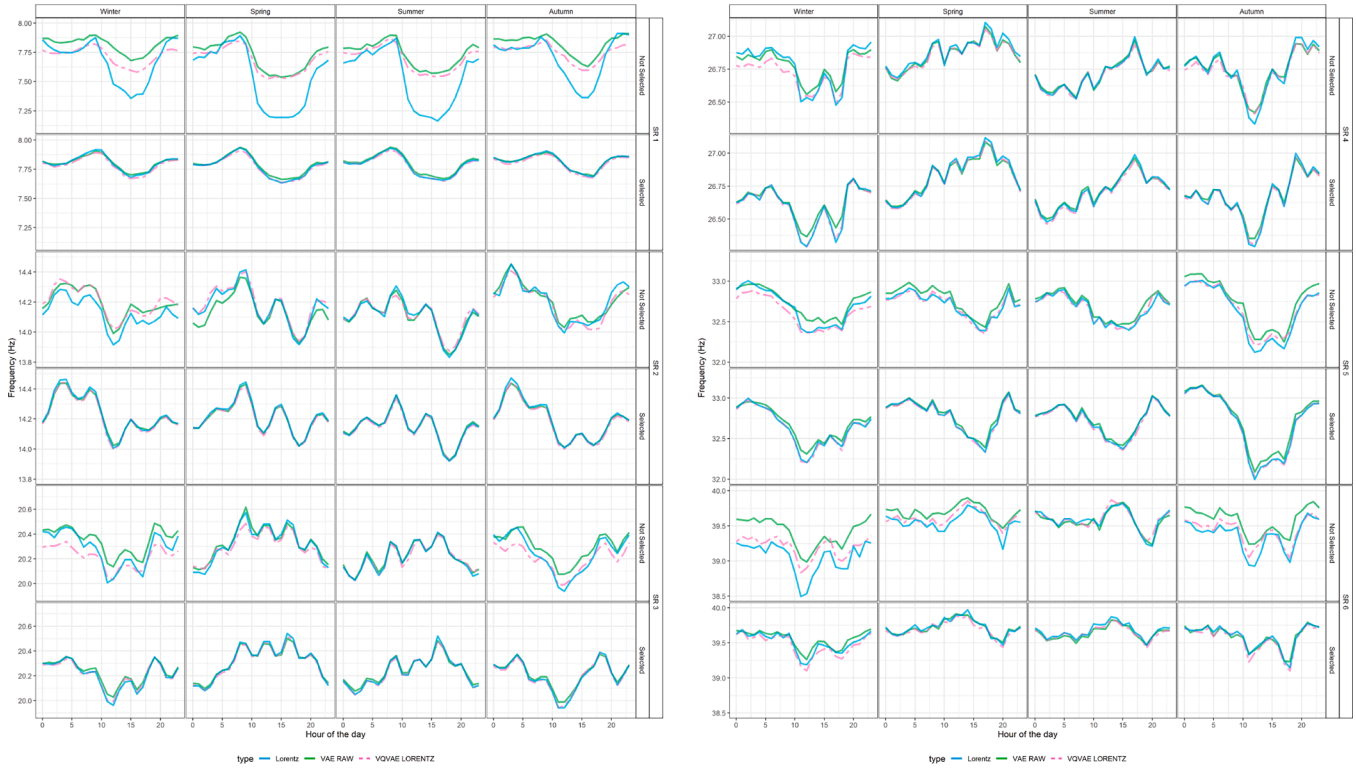

(a) (b)

Fig. 9. Diurnal variation, separated by each of the four seasons: LCF versus VAE Raw and VQVAE Lorentz. **(a)** 1st–3rd SR modes, **(b)** 4th–6th SR modes.

jointly learning signal representations (via reconstruction) rather than optimizing solely for frequency prediction.

6.1. Experimental setup

We train a CNN on the same data set of low-noise signals originally used for the AE training. Following standard practice for regression tasks with this paradigm, the final layer outputs a single predicted frequency. In opposition, our proposed VAE method learns a latent representation while reconstructing the input signals. By preserving critical features (including the frequency content) through reconstruction, the VAE benefits from an additional objective beyond direct frequency regression, thereby making it more robust to noise. To evaluate generalization ability, we test both models on a highly noisy data set, which better represents the challenging real-world conditions that deviate substantially from the low-noise domain of the training data.

6.2. Error comparison

We compare the model outputs against ground-truth frequencies using several criteria.

6.2.1. Distribution similarity

We examine how closely the predicted frequency distributions match the true distribution. As illustrated in Fig. 10, the direct

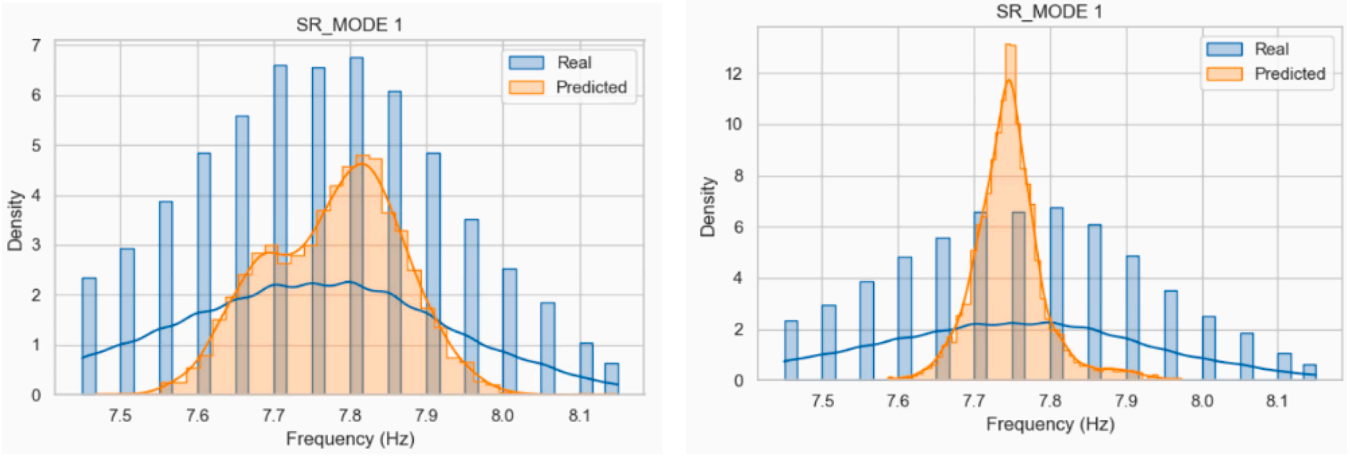

(a) Conv1D (Raw Input) (b) Conv1D (Lorentz Input)

Fig. 10. Distribution of frequency estimations (LCF vs. CNN predictions). (a) uses the raw input signal, while (b) employs a Lorentz-based preprocessed input.

Table 4
Comparison of KS statistics across architectures and input representations.

SR MODE	VAE	Conv1D-Raw	Conv1D-Lorentz	Ref.
SR1	0.094	0.243	0.360	0.220
SR2	0.100	0.271	0.142	0.096
SR3	0.054	0.163	0.169	0.039
SR4	0.056	0.129	0.141	0.071
SR5	0.037	0.241	0.150	0.066
SR6	0.085	0.382	0.362	0.075

frequency-estimation approach (CNN) appears to capture the overall frequency distribution reasonably well. Between the two CNN variants – one using raw data (Fig. 10(a)) and one using Lorentz-processed data (Fig. 10(b) – the raw-data variant displays slightly less variability, suggesting marginally better performance in certain regions.

6.2.2. Numerical metrics

Table 4 reports the Kolmogorov–Smirnov (KS) statistics for both CNN variants (Conv1D-Raw and Conv1D-Lorentz), our VAE (LORENTZ) approach, and a reference (Ref.) method using a Lorentz curve fit. Lower KS values indicate a closer match to the ground-truth distribution. Our VAE achieves consistently low KS values across different scenarios, demonstrating superior robustness in the presence of noise.

Our experiments indicate that training a CNN solely on low-noise data restricts its ability to generalize to higher-noise environments. By contrast, the VAE leverages a latent representation that must also reconstruct the original signal. This additional objective encourages the model to learn more robust features, leading to improved performance even under challenging conditions. Furthermore, the latent encoding derived from the VAE offers valuable by-products for downstream tasks, such as event detection, system-state characterization, or anomaly identification. While the CNN focuses exclusively on frequency prediction, the VAE broader learned representation can thus serve multiple diagnostic and monitoring purposes. Hence, the VAE-based approach consistently exhibits high fidelity across both optimal and worst-case scenarios, surpassing purely frequency-focused CNN methods. These findings underscore the importance of learning richer representations of the underlying signal structure, rather than relying solely on direct frequency regression.

7. Discussions

The general findings of the experiments following our initial assumptions are discussed in the following lines. In the second part of this section, a projection of several practical areas for further application of the generalizable proposed framework is also presented.

7.1. Limitations

One important restriction lies in our reliance on the LCF process to generate the “ground truth” data for training and validation. Although we adopt the VAE framework precisely because it can handle more variability and noise, our model’s performance ultimately depends on the accuracy of these LCF-derived references during training. In scenarios where the LCF fit is less reliable—even for moderate noise levels—its inaccuracies can propagate through our pipeline, affecting both the latent representation and the final frequency estimates.

A second limitation stems from the fact that SR stations can exhibit distinctly different noise profiles, local interferences, and instrumentation setups. As a result, our current model requires station-specific fine-tuning to adapt to each environment’s unique characteristics. While this ensures more precise frequency extraction at each station, it also reduces the “plug-and-play” nature of our approach and increases the effort required when deploying it across multiple stations or when station conditions change over time.

Finally, while our VAE-based method has proven robust at denoising signals and extracting multiple SR modes, the first mode remains especially challenging under strong noise conditions. Although our latent-space encoding appears to capture essential features of the SR spectrum even in the presence of elevated noise, the accuracy of the first-mode frequency extraction can be notably lower than in cleaner data. Ongoing and future efforts will focus on refining the model architecture and loss functions to further strengthen its resilience in these most difficult scenarios.

7.2. Possible applications

The enhanced capability of our hybrid DL methodology to extract multiple SR modes beyond the third opens up a wide range of applications in geophysical research. Traditionally, the LCF algorithm has been limited to reliably extracting only the first three SR modes, due to the mathematical complexity of fitting procedures over the noisy, highly variable signals. This limitation has masked potential relationships between SR and various natural events that manifest in higher-order modes. Our methodology overcomes these challenges, thus allowing the analysis of more complex links with such phenomena. In the following, we illustrate scenarios in which the proposed methodology can be successfully utilized.

Using only the LCF, the extraction of higher SR modes associated with preseismic ionospheric anomalies has been problematic. Higher modes could provide more information and improve the localized changes in the ionosphere caused by stress accumulation in the Earth’s crust prior to seismic events. Our hybrid technique could enable the reliable extraction of these, potentially revealing subtle preseismic signatures that were previously undetectable.

Small changes in the ionospheric conductivity profile, caused by factors such as solar radiation, geomagnetic storms, or atmospheric tides, can affect the propagation characteristics of SR signals. Solar events like solar flares and coronal mass ejections significantly impact the Earth’s ionosphere, altering its conductivity and affecting SR signals. Our improved approach would facilitate the extraction of critical information contained in higher modes, providing a more comprehensive view of how these activities influence the ionosphere and enhancing models that predict space weather effects on communication and navigation systems.

Atmospheric events such as thunderstorms and lightning activity influence the global electrical circuit and consequently the SR signals. The ability of the methodology to extract additional modes would enable researchers to investigate the relationship between atmospheric electrical activity and SR signals more thoroughly, improving our understanding of atmospheric-ionospheric coupling processes.

8. Conclusions and future work

This papers brings a new methodology as an alternative to the traditional LCF for SR signal analysis. The novel DL tool reduces the dimension of the SR frequency spectrum and includes a new regression layer in the learned space that allows the simultaneous extraction of the central values of the first six modes of the signal.

The proposed DL approach offers significant advantages over the canonical LCF method. While the LCF is effective under ideal conditions with low noise levels, it often struggles with noisy data, leading to inaccurate frequency estimations and misidentification of SR modes, especially beyond the third mode. In contrast, our DL model demonstrates robust performance across varying noise levels, effectively denoising the input signals and accurately reconstructing the SR modes. The ability of our model to maintain high accuracy in frequency estimation, even in extremely noisy conditions where the LCF fails, highlights the strength of the constructed methodology. Furthermore, by reducing the reliance on fitting procedures that are sensitive to noise and data variability, our approach provides a more reliable and comprehensive

analysis of SR data. This not only enhances the quality of the extracted features but also enables the inclusion of previously discarded segments, thereby expanding the set available for research. The innovative aspect of our method lies in its capacity to overcome the limitations of existing techniques, offering improved accuracy, robustness, and applicability in the analysis of SR signals under challenging conditions.

Moreover, our DL model exhibits the capability to discern patterns depending on the hour and the season, generating the same number of peaks at corresponding times as the LCF algorithm. In almost all modes, the frequency values interval shows far greater similarities between the previously selected and non-selected registers when using the DL architecture. This consistency indicates that our methodology effectively captures the intrinsic characteristics of the SR signals across different temporal conditions. These results have further strengthened our confidence in the use of DL autoencoders to enhance the LCF function. With this new methodology, registers that have previously been rejected due to high noise levels can now be considered for analysis. This inclusion leads to the recovery of a large amount of previously unusable ELF data, significantly increasing the volume of samples available for SR research and potential applications. Using these additional data points, researchers can perform more comprehensive studies, leading to deeper insights and advances in understanding geophysical phenomena.

The presented DL approach is also computationally efficient, due to the optimized architecture of the autoencoder, allowing effective processing of SR data without excessive computational demands.

Although the model has been developed and tested using samples from a single station, assessing its generalization capabilities is an important aspect of our future work. We plan to test the model on different data sets and under varying conditions to evaluate its robustness across diverse scenarios. By fine-tuning the approach to accommodate the specific characteristics of each station, we aim to demonstrate its adaptability and effectiveness in analyzing SR signals from multiple sources.

CRediT authorship contribution statement

Carlos Cano-Domingo: Conceptualization, Methodology, Software, Investigation, Writing – original draft, Visualization; **Ruxandra Stoean:** Conceptualization, Validation, Investigation, Writing – review & editing; **Gonzalo Joya:** Conceptualization, Validation, Formal analysis; **Nuria Novas:** Resources, Data curation, Validation; **Manuel Fernández-Ros:** Resources, Data curation, Validation; **Jose A. Gázquez Parra:** Resources, Data curation, Validation.

Data availability

Data will be made available on request.

Declaration of competing interest

The authors declare the following financial interests/personal relationships which may be considered as potential competing interests:

Ruxandra Stoean reports financial support was provided by Romanian Ministry of Research and Innovation. Carlos Cano-Domingo reports administrative support and equipment, drugs, or supplies were provided by University of Malaga. Ruxandra Stoean reports financial support was provided by CETPartnership, the European Partnership under Joint Call 2022 for research proposals, co-funded by the European Commission. Carlos Cano-Domingo reports administrative support was provided by CETPartnership, the European Partnership under Joint Call 2022 for research proposals, co-funded by the European Commission. Nuria Novas reports financial support was provided by Andalusian Institute of Geophysics, The Ministry of Economics and Competitiveness of Spain. Manuel Fernandez-Ros reports financial support was provided by Andalusian Institute of Geophysics, The Ministry of Economics and Competitiveness of Spain. Jose A. Gazquez Parra reports financial support was provided by Andalusian Institute of Geophysics, The Ministry of Economics and Competitiveness of Spain. Nuria Novas reports financial support was provided by European Union FEDER Program and CIAMBITAL Group. Manuel Fernandez-Ros reports financial support was provided by European Union FEDER Program and CIAMBITAL Group by. Jose A. Gazquez Parra reports financial support was provided by European Union FEDER Program and CIAMBITAL Group. If there are other authors, they declare that they have no known competing financial interests or personal relationships that could have appeared to influence the work reported in this paper.

Acknowledgments

R. Stoean was supported by the Romanian Ministry of Research and Innovation, CCCDI—UEFISCDI, project number 178PCE/2021, PN-III-P4-ID-PCE-2020-0788, within PNCDI III. C. Cano was partially supported by a stay at the Electronics Technology Department of the University of Málaga. This research was also funded by CETPartnership, the European Partnership under Joint Call 2022 for research proposals, co-funded by the European Commission (GA no. 101069750) and with the funding organisations listed on the CETPartnership website, project number COFUND-CETP 40/2024, UEFISCDI PNCDI IV. We also thank the Andalusian Institute of Geophysics. The Ministry of Economics and Competitiveness of Spain financed this work, under Project TEC2014-60132-P, in part by Innovation, Science and Enterprise, Andalusian Regional Government through the Electronics, Communications, and Telemedicine TIC019 Research Group of the University of Almeria, Spain and in part by the European Union FEDER Program and CIAMBITAL Group by I + D + I Project UAL18-TIC-A025-A, the University of Almeria, and the European Regional Development Fund (FEDER).

References

Berger, V. W., & Zhou, Y. (2014). Kolmogorov–Smirnov test: Overview. *Wiley Statsref: Statistics Reference Online*. https://doi.org/10.1002/9781118445112.stat06558

Boldi, R., Williams, E., & Guha, A. (2018). Determination of the global-average charge moment of a lightning flash using Schumann resonances and the LIS/OTD lightning data. *Journal of Geophysical Research: Atmospheres*, *123*(1), 108–123. https://doi.org/10.1002/2017JD027050

Bozóki, T., Sátori, G., Williams, E., Mironova, I., Steinbach, P., Bland, E. C., Koloskov, A., Yampolski, Y. M., Budanov, O. V., Neska, M., Sinha, A. K., Rawat, R., Sato, M., Beggan, C. D., Toledo-Redondo, S., Liu, Y., & Boldi, R. (2021). Solar cycle-modulated deformation of the Earth–ionosphere cavity. *Frontiers in Earth Science*, *9*. https://doi.org/10.3389/feart.2021.689127

Cano-Domingo, C., Fernandez-Ros, M., Novas-Castellano, N., & Gazquez-Parra, J. A. (2021). Diurnal and seasonal results of the Schumann resonance observatory in Sierra de Filabres, Spain. *IEEE Transactions on Antennas and Propagation*, (pp. 1–10). https://doi.org/10.1109/TAP.2021.3069537

Cano-Domingo, C., Novas-Castellano, N., Fernandez-Ros, M., & Gazquez-Parra, J. A. (2022). Segmentation and characteristic extraction for Schumann resonance transient events. *Measurement*, *194*, 110957. https://doi.org/10.1016/j.measurement.2022.110957

Cano-Domingo, C., Stoean, R., Joya, G., Novas-Castellano, N., Fernandez-Ros, M., & Gazquez-Parra, J. A. (2023). A machine learning hourly analysis on the relation the ionosphere and Schumann resonance frequency. *Measurement*, *208*, 112426. https://doi.org/10.1016/j.measurement.2022.112426

Contopoulos, I., Mlynarczyk, J., Kubisz, J., & Tritakis, V. (2024). Possible identification of precursor ELF signals on recent EQs that occurred close to the recording station. *Atmosphere*, *15*(9). https://doi.org/10.3390/atmos15091134

Figueredo, P. S., Ortega, B. M., Pazos, M., Osorio, D. R., Mascote, E. A., Mendoza, V. M., & Garduño, R. (2021). Schumann resonance anomalies possibly associated with large earthquakes in Mexico. *Indian Journal of Physics*, *95*, 1959–1966. https://doi.org/10.1007/s12648-020-01865-6

Fime, A. A., Ashikuzzaman, M., & Aziz, A. (2024). Audio signal based danger detection using signal processing and deep learning. *Expert Systems with Applications*, *237*, 121646. https://doi.org/10.1016/j.eswa.2023.121646

Galuk, Y. P., Kudintseva, I. G., Nickolaenko, A. P., & Hayakawa, M. (2020). Modifications of Schumann resonance spectra as an estimate of causative earthquake magnitude: The model treatment. *Journal of Atmospheric and Solar-Terrestrial Physics*, *209*, 105392. https://doi.org/10.1016/j.jastp.2020.105392

Ganguly, B., & Dey, D. (2024). An improved time-frequency representation aided deep learning framework for automated diagnosis of sleep apnea from ECG signals. *Measurement*, (p. 116170). https://doi.org/10.1016/j.measurement.2024.116170

Gao, C., Zhao, P., Fan, Q., Jing, H., Dang, R., Sun, W., Feng, Y., Hu, B., & Wang, Q. (2023). Deep neural network: As the novel pipelines in multiple preprocessing for Raman spectroscopy. *Spectrochimica Acta Part A: Molecular and Biomolecular Spectroscopy*, *302*, 123086. https://doi.org/10.1016/j.saa.2023.123086

Gao, F., Li, B., Chen, L., Wei, X., Shang, Z., & He, C. (2020). Ultrasonic signal denoising based on autoencoder. *Review of Scientific Instruments*, *91*. https://doi.org/10.1063/1.5136269

Guha, A., Williams, E., Boldi, R., Sátori, G., Nagy, T., Bór, J., Montanyà, J., & Ortega, P. (2017). Aliasing of the Schumann resonance background signal by sprite-associated Q-bursts. *Journal of Atmospheric and Solar-Terrestrial Physics*, *165–166*, 25–37. https://doi.org/10.1016/j.jastp.2017.11.003

Gázquez Parra, J. A., Ros, M. F., Castellano, N. N., & Salvador, R. M. G. (2015). Techniques for Schumann resonance measurements: A comparison of four amplifiers with a noise floor estimate. *IEEE Transactions on Instrumentation and Measurement*, *64*(10), 2759–2768. https://doi.org/10.1109/TIM.2015.2420376

Hayakawa, M., Izutsu, J., Schekotov, A. Y., Nickolaenko, A. P., Galuk, Y. P., & Kudintseva, I. G. (2021). Anomalies of Schumann resonances as observed near Nagoya associated with two huge (M7) Tohoku offshore earthquakes in 2021. *Journal of Atmospheric and Solar-Terrestrial Physics*, *225*, 105761. https://doi.org/10.1016/j.jastp.2021.105761

Hetita, I., Zalhaf, A. S., Mansour, D.-E. A., Han, Y., Yang, P., & Wang, C. (2022). Accurate modeling of photovoltaic systems for studying the transient effects of lightning strikes. *Energy Reports*, *8*, 429–438. 2021 The 8th International Conference on Power and Energy Systems Engineering. https://doi.org/10.1016/j.egyr.2021.11.111

Kim, C. H., Ahn, S., Chae, K. Y., Hooker, J., & Rogachev, G. V. (2023). Restoring original signals from pile-up using deep learning. *Nuclear Instruments and Methods in Physics Research Section A: Accelerators, Spectrometers, Detectors and Associated Equipment*, *1055*, 168492. https://doi.org/10.1016/j.nima.2023.168492

Koloskov, A. V., Nickolaenko, A. P., Yampolsky, Y. M., Hall, C., & Budanov, O. V., et al. (2020). Variations of global thunderstorm activity derived from the long-term Schumann resonance monitoring in the Antarctic and in the Arctic. *Journal of Atmospheric and Solar-Terrestrial Physics*, *201*(February), 105231. https://doi.org/10.1016/j.jastp.2020.105231

Kudintseva, I. G., Galuk, Y. P., Nickolaenko, A. P., & Hayakawa, M. (2018). Modifications of middle atmosphere conductivity during sudden ionospheric disturbances deduced from changes of Schumann resonance peak frequencies. *Radio Science*, *53*(5), 670–682. https://doi.org/10.1029/2018RS006554

Li, P., Pei, Y., & Li, J. (2023). A comprehensive survey on design and application of autoencoder in deep learning. *Applied Soft Computing*, *138*, 110176. https://doi.org/10.1016/j.asoc.2023.110176

Maddams, W. F. (1980). The scope and limitations of curve fitting. *Applied Spectroscopy*, *34*, 245–267. https://doi.org/10.1366/0003702804730312

Mohagheghian, F., Han, D., Ghetia, O., Chen, D., Peitzsch, A., Nishita, N., Ding, E. Y., Mensah Otabil, E., Noorishirazi, K., Hamel, A., Dickson, E. L., DiMezza, D., Tran, K.-V., McManus, D. D., & Chon, K. H. (2024). Atrial fibrillation detection on reconstructed photoplethysmography signals collected from a smartwatch using a denoising autoencoder. *Expert Systems with Applications*, *237*, 121611. https://doi.org/10.1016/j.eswa.2023.121611

Mushtak, V. C., & Williams, E. R. (2009). An improved Lorentzian technique for evaluating resonance characteristics of the Earth-ionosphere cavity. *Atmospheric Research*, *91*, 188–193. https://doi.org/10.1016/j.atmosres.2008.08.013

Nickolaenko, A. P., Galuk, Y. P., & Hayakawa, M. (2024). Terminator effect in the model Schumann resonance signals. *Journal of Atmospheric and Solar-Terrestrial Physics*, *256*, 106195. https://doi.org/10.1016/j.jastp.2024.106195

Ondrášková, A., & Ševčík, S. (2014). The iterative complex demodulation applied on short and long Schumann resonance measured sequences. *Contributions to Geophysics and Geodesy*, *44*, 313–328. https://doi.org/10.1515/congeo-2015-0008

Oppliger, J., Denner, M. M., Küspert, J., Frison, R., Wang, Q., Morawietz, A., Ivashko, O., Dippel, A. C., von Zimmermann, M., Biało, I., Martinelli, L., Fauqué, B., Choi, J., Garcia-Fernandez, M., Zhou, K. J., Christensen, N. B., Kurosawa, T., Momono, N., Oda, M., …, Chang, J. (2024). Weak signal extraction enabled by deep neural network denoising of diffraction data. *Nature Machine Intelligence*, *6*. https://doi.org/10.1038/s42256-024-00790-1

Pamukti, B., Wang, Z., Fajar Faliasthiunus Pradipta, M., Liaw, S.-K., Yeh, C.-H., & Yang, F.-L. (2024). Deep learning and time series signal processing for bending detection in mining environment using optical fiber sensor. *Optical Fiber Technology*, *88*, 103819. https://doi.org/10.1016/j.yofte.2024.103819

Perotoni, M. B. (2018). Eigenmode prediction of the Schumann resonances. *IEEE Antennas and Wireless Propagation Letters*, *17*(6), 942–945. https://doi.org/10.1109/LAWP.2018.2825398

Pizzuti, A., Bennett, A., & Füllekrug, M. (2022). Long-term observations of Schumann resonances at Portishead (UK). *Atmosphere*, *13*. https://doi.org/10.3390/atmos13010038

Price, C. (2016). ELF electromagnetic waves from lightning: The Schumann resonances. *Atmosphere*, *7*(9). https://doi.org/10.3390/atmos7090116

Purwins, H., Li, B., Virtanen, T., Schlüter, J., Chang, S. Y., & Sainath, T. (2019). Deep learning for audio signal processing. *IEEE Journal on Selected Topics in Signal Processing*, *13*, 206–219. https://doi.org/10.1109/JSTSP.2019.2908700

Qiu, S., Wang, Z., Lu, G., Zhima, Z., Soon, W., Manue, V., Herrera, V., & Ju, P. (2024). First observations of the transient luminous event effect on ionospheric Schumann resonance, based on the China seismo-electromagnetic satellite. *Atmospheric Chemistry and Physics*, *24*(14), 8519–8527. https://doi.org/10.5194/acp-24-8519-2024

Qu, Z., Wang, W., Hou, C., & Hou, C. (2019). Radar signal intra-pulse modulation recognition based on convolutional denoising autoencoder and deep convolutional neural network. *IEEE Access*, *7*, 112339–112347. https://doi.org/10.1109/ACCESS.2019.2935247

Ribeiro, A. H., Horta Ribeiro, M., Paixão, G., Oliveira, D., Gomes, P., Canazart, J., Ferreira, M., Andersson, C., Macfarlane, P., Meira, Jr., W., Schön, T., & Ribeiro, A. L. (2020). Automatic diagnosis of the 12-lead ECG using a deep neural network. *Nature Communications*, *11*. https://doi.org/10.1038/s41467-020-15432-4

Rodríguez-Camacho, J., Salinas, A., Carrión, M., Portí, J., Fornieles-Callejon, J., & Toledo-Redondo, S. (2022). Four year study of the Schumann resonance regular variations using the Sierra Nevada station ground-based magnetometers. *Journal of Geophysical Research: Atmospheres*, *127*. https://doi.org/10.1029/2021JD036051

Schumann, W. O. (1952). Über die strahlungslosen eigenschwingungen einer leitenden kugel, die von einer luftschicht und einer ionosphärenhülle umgeben ist (*English translation*: On the radiation-free natural oscillations of a conducting sphere surrounded by an air layer and an ionospheric shell). *Zeitschrift fur Naturforschung - Section A Journal of Physical Sciences*, *7*(2), 149–154. https://doi.org/10.1515/zna-1952-0202

Sentman, D. D. (1987). Magnetic elliptical polarization of Schumann resonances. *Radio Science*, *22*. https://doi.org/10.1029/RS022i004p00595

Shvets, A., Hobara, Y., Hayakawa, M., Shvets, A., Koloskov, O., & Yampolsky, Y. (2024). Investigation of anomalous lightning activity during the January 15, 2022 Tonga volcano eruption based on measurements of the VLF and ELF electromagnetic fields. *Journal of Atmospheric and Solar-Terrestrial Physics*, *264*. https://doi.org/10.1016/j.jastp.2024.106344

Stoean, C., Stoean, R., Atencia, M., Abdar, M., Velázquez-Pérez, L., Khosravi, A., Nahavandi, S., Acharya, U. R., & Joya, G. (2020). Automated detection of presymptomatic conditions in spinocerebellar ataxia type 2 using Monte Carlo dropout and deep neural network techniques with electrooculogram signals. *Sensors*, *20*(11). https://doi.org/10.3390/s20113032

Tatsis, G., Sakkas, A., Christofilakis, V., Baldoumas, G., Chronopoulos, S. K., Paschalidou, A. K., Kassomenos, P., Petrou, I., Kostarakis, P., Repapis, C., & Tritakis, V. (2021). Correlation of local lightning activity with extra low frequency detector for Schumann resonance measurements. *Science of the Total Environment*, *787*. https://doi.org/10.1016/j.scitotenv.2021.147671

Ul Amin, S., Kim, B., Jung, Y., Seo, S., & Park, S. (2024). Video anomaly detection utilizing efficient spatiotemporal feature fusion with 3D convolutions and long short-term memory modules. *Advanced Intelligent Systems*, *6*(7), 2300706. https://doi.org/10.1002/aisy.202300706

Wu, H., & Flierl, M. (2020). Vector quantization-based regularization for autoencoders. In *Aaai conference on artificial intelligence* (pp. 6380–6387). https://doi.org/10.1609/aaai.v34i04.6108

Yang, J., Xu, J., Zhang, X., Wu, C., Lin, T., & Ying, Y. (2019). Deep learning for vibrational spectral analysis: Recent progress and a practical guide. *Analytica Chimica Acta*, *1081*, 6–17. https://doi.org/10.1016/j.aca.2019.06.012